Science Robotics
AAAS

Supplementary Materials for

A self-rotating, single-actuated UAV with extended sensor field of view for autonomous navigation

Nan Chen *et al.*

Corresponding author: Fu Zhang, fuzhang@hku.hk

Sci. Robot. **8**, eade4538 (2023)
DOI: 10.1126/scirobotics.ade4538

The PDF file includes:

Other Supplementary Material for this manuscript includes the following:

Supplementary Text

Section S1. Hardware installation and setup of the magnetic encoder

The magnetic encoder consists of two parts: one small magnet and an encoder chip (Fig. S1B). The small magnet is attached to the motor shaft by glue (Fig. S1C) and the encoder chip is placed right below the motor shaft (Fig. S1D). Motor rotation produces a rotating magnetic field via the small magnet, whose rotation angle is sensed by the encoder chip. The encoder chip has two ports, one for chip configuration and the other for angle measurements output (Fig. S1A). Based on instructions from the chip user manual, we specified the angle zero and configured its output mode as a 910-Hz PWM output. In this mode, the duty cycle of the output PWM represents the rotor angle (the lowest duty cycle represents an angle of 0° and the highest duty cycle represents an angle of 360°). The PWM output of the encoder chip is fed to the flight controller (MCU STM32F765), whose PWM input port is configured as a PWM capture mode. In this way, the flight controller can capture the received duty cycle hence the measured rotor angle. We also adapted the PX4 Autopilot to read the data on the PWM port.

Section S2. Selection of PULSAR's propeller and motor

PULSAR uses commercial off-the-shelf motors and propellers to ease its implementation. For the propellers, its size range is first determined approximately according to the total weight of PULSAR. Since we should connect the propeller blades to the swashplateless mechanism, a foldable propeller where the two blades are separated is preferred. These considerations eventually lead to a 13-inch T-MOTOR MF1302 propeller for PULSAR. After connecting the blades to the swashplateless mechanism, the total diameter of the propeller is 14.8 inches (37.6 cm). Then, we test the propeller integrated with the swashplateless mechanism on the test stand (Fig. S7A(i)), and obtained the propeller drag coefficient $C_Q = 9.212 \times 10^{-7}$ Nm/(rad/s)^2. Further, we assemble a typical motor rotor with the propeller in SolidWorks software and calculate the rotor inertia J with appropriate material density, obtaining $J = 1.296 \times 10^{-4}$ kg·m^2.

With the chosen propeller and the determined rotor parameter, the next is to select a proper motor. To achieve fast cyclic pitch angle adjustment for the blades, a motor capable of providing large acceleration should be used. Since the motor armature inductance is typically very small and the frequency of the modulated sinusoidal throttle (same as the motor rotation frequency) is much lower than that of the driving signal on each motor phase (same as the motor electrical frequency which is equal to the motor rotation frequency times the number of pole-pairs), the motor armature inductance can be ignored, leading to a first order motor dynamics as below

$$U = \frac{JR}{K_e}\dot{\sigma} + \frac{C_Q R}{K_e}\sigma^2 + K_e\sigma \tag{S1}$$

where U is the motor input voltage, R is the armature resistance, $K_e = 30/(\pi K_v)$ with K_v being the motor velocity constant in rpm/V, and σ is the motor speed.

By linearizing Eq. S1 at its operating point, the hovering speed σ_h, and applying the Laplace

transform, a transfer function can be obtained as

$$\frac{\Delta\sigma}{\Delta U} = \frac{\frac{K_e}{2RC_Q\sigma_h + K_e^2}}{\frac{J}{2C_Q\sigma_h + K_e^2/R}s + 1} = \frac{g_{dc}}{\tau s + 1}. \tag{S2}$$

where $g_{dc} = K_e/(2RC_Q\sigma_h + K_e^2)$ is the static gain indicating the gain of the speed change in response to constant voltage change and $\tau = J/(2C_Q\sigma_h + K_e^2/R)$ is the time constant indicating the response delay. According to the working principle of swashplateless mechanism, the modulated voltage change ΔU is the sinusoidal throttle whose frequency is the same as the rotor frequency. Hence, the gain of the transfer function in Eq. S2 at that rotor frequency is most interesting. Specifically, we focus on the hovering condition, where the rotor frequency is around 4700 rpm (i.e., 492 rad/s), we call the gain at this frequency the hovering gain, $g_h = g_{dc}/(\tau \cdot \sigma_h + 1)$. To select a motor for better performance of swashplateless mechanism, we should choose the suitable armature resistance R and the value of K_v to maximize the hovering gain g_h, such that the rotor speed response (hence the moment induced by the swashplateless mechanism) is maximized. Furthermore, if the hovering gains are similar, the motor with higher voltage input range (i.e., allowed maximum battery cells) is preferred since it allows a larger range of ΔU which also leads to higher moments on the swashplateless mechanism. Based on these analyses, we evaluated eleven off-the-shelf motors (Table S2) and chose T-MOTOR MN5006 KV450, which achieved the highest hovering gain of 5.50 rad/s/V and allows 6S batteries.

Section S3. Evaluation of swashplateless mechanism

To evaluate the performance of the designed swashplateless mechanism, it was fixed to a test stand through a 6D force sensor and the results are shown in Fig. S2. The moment increases with both the average throttle and the amplitude of the sinusoidal throttle, and the maximum controllable moment is close to 0.8 Nm, which is sufficient for micro UAV control. Moreover, the deadband phenomenon widely existing in the original design (*35*) is resolved with the bearing design and pressure bearing, which mitigate the friction during high-frequency rotation substantially. Consequently, the moment increases smoothly with the sinusoidal throttle amplitude. The relation can be well approximated as linear, which improves the system linearity and hence control performance. On the other hand, the thrust is linear to the average throttle and is not obviously affected by the sinusoidal throttle amplitude, which effectively decouples the thrust and moment and simplifies the overall control design.

Section S4. The benchmarked quadrotors

Here we present the selection of motors and propellers for the benchmarked quadrotors.

Selection of the quadrotor's propeller

Since the propeller diameter of PULSAR is 37.6 cm (14.8 inches), to keep the same total disk area, a 7.5-inch propeller is most suitable for a quadrotor for the comparison study. However, there are only a few options for off-the-shelf 7.5-inch propellers. Hence, off-the-shelf 8-inch propellers are also considered although it gives the quadrotor unfair advantages due to the larger

disk area. We evaluate nine propellers from three mainstream brands that can provide the propellers in the diameter we needed (i.e., GAMFAN, HQProp, and APC) and choose the best one of them. Since the propeller and motor cannot be tested separately, to determine the best propeller and motor, we follow a two-step procedure: first, we test the nine propellers with two candidate motors and choose the best propeller; Second, we fix the best propeller chosen in the first step and enumerate more motors to select the best motor.

In the first step, we use candidate motors to evaluate and select the best propeller. We choose two candidate motors that are suitable for common 7.5-inch and 8-inch propellers and that have very different KV values. The chosen candidate motors are SUNNYSKY V2806 (KV650) and T-Motor F90 (KV1300). The power efficiencies of the nine propellers when driven by the two candidate motors are shown in Fig. S3. The results indicate that for both motors, the best propellers are GAMFAN 7535 (for 7.5-inch propellers) and GAMFAN 8040 (for 8-inch propellers), respectively.

Selection of the quadrotor's motor

In the second step, we fix the best propeller in each size (i.e., GAMFAN7535 for 7.5-inch propeller and GAMFAN8040 for 8-inch propeller) and evaluate more motors to select the best one. First, we select motors of two mainstream brands with various sizes and KV values. Since motors with KV values higher than 1300 are not suitable for propellers larger than 7 inches, we only consider motors with KV values below 1300. This criterion gives us six motors: V2806 (KV650) and V3506 (KV650) from SUNNYSKY, and F90 (KV1300), V2812 (KV925), MN2806 (KV650), and MN5006 (KV450) from T-MOTOR.

With all the motors, we test each of them with the best propeller in each size. The results are shown in Fig. S4. As can be seen, when providing a thrust in the range of 300-400 g, the SUNNYSKY V3506 has the best efficiency and a weight of 84 g, SUNNYSKY V2806 has the next best efficiency and a weight of 47 g, and T-MOTOR MN2806 has the third best efficiency and a weight of 46 g. Since SUNNYSKY V2806 has an efficiency very close to the best one SUNNYSKY V3506 but with a much smaller weight (47 g versus 84 g), we decide to use SUNNYSKY V2806. It is also noted that the MN5006 motor (the motor for PULSAR) has a very different trend when used with the 7.5-inch and 8-inch propellers compared with other motors, this is because the motor has a relatively large size, blocking much area of the propeller disk when the propeller diameter is small.

The quadrotors for comparison

With the selected propulsion systems, this section constructs the two quadrotors (one has 7.5-inch propellers, and the other has 8-inch propellers). When constructing the quadrotors, we minimize the overall vehicle size to prevent too large quadrotor sizes from causing unfair comparison with PULSAR. Moreover, the quadrotors carry the same avionic payloads (including the flight controller board, companion computer, and LiDAR sensors) and battery, which are shown in Table S3. The table also details the weight of the propulsion systems of the two quadrotors and PULSAR. Since the quadrotors have more motors, propellers, and ESCs, the propulsion system weighs 159 g more than that of PULSAR. In addition, since the quadrotors have four motors distributed on four arms, it requires longer wires and more structure materials, contributing to 47 g more weight. As a result, the total weight of the two quadrotors is 206 g more than that of PULSAR. Finally, the two constructed quadrotors are shown in Fig. S5.

Section S5. Efficiency analysis

Analysis according to momentum theory

According to momentum theory (*39*), for a single propeller, the total power P and static thrust T have the relation as

$$P = \sqrt{\frac{T^3}{2\rho A}} \tag{S3}$$

where ρ is the density of air and A is propeller area. The power efficiency η is defined as thrust per unit of power, as follows

$$\eta = \frac{T}{P} \tag{S4}$$

Selecting propeller diameters of PULSAR and the quadrotor such that

$$D_{\text{pulsar}} = 2D_{\text{quad}} = L \tag{S5}$$

Then, we can obtain the total disk area for the quadrotor $A_{\text{quad}} = 4\pi(D_{\text{quad}}/4)^2 = \pi L^2/4$, which is the same as that of PULSAR $A_{\text{pulsar}} = \pi(D_{\text{pulsar}}/2)^2 = \pi L^2/4$ as required. If the thrusts supplied by PULSAR and the quadrotor are the same, i.e., $T_{\text{pulsar}} = T_{\text{quad}} = T$, then their power efficiency are

$$\eta_{\text{pulsar}} = \frac{T_{\text{pulsar}}}{P_{\text{pulsar}}} = \frac{T}{\sqrt{\frac{T^3}{2\rho A_{\text{pulsar}}}}} = \sqrt{\frac{\rho\pi L^2}{2T}} \tag{S6}$$

and

$$\eta_{\text{quad}} = \frac{T_{\text{quad}}}{P_{\text{quad}}} = \frac{T}{4\sqrt{\frac{(T/4)^3}{2\rho(A_{\text{quad}}/4)}}} = \sqrt{\frac{\rho\pi L^2}{2T}} \tag{S7}$$

which means PULSAR and the quadrotor have the same power efficiency when the provided thrusts and total propeller disk areas are the same.

In practice, momentum theory has many ideal hypotheses, for example, the propeller is assumed to be an infinitesimally thin actuator disc and the actuator disc is uniformly loaded, etc. (*39*). Hence, the efficiency calculated by momentum theory is the ideal (i.e., the upper limit) efficiency that a real propeller cannot achieve in practice. Next, we verify the power efficiency predicted by momentum theory using actual propeller data.

Evaluation by APC's propeller database

We use the data from the APC's propeller database (*61*) to verify the efficiency comparison between one big propeller and four smaller propellers as predicted by momentum theory above. The database contains detailed specifications, including the power, thrust, torque of various APC propellers (528 in total) of different sizes (from 4 inches to 28 inches) and operation conditions (e.g., rotation speed, airspeed). These data are obtained by high-fidelity simulation based on the more advanced vortex theory (*62, 63*) using actual propeller geometry.

To conduct the comparison, we first select propellers with integer diameters in the range from 4 to 18 inches, beyond which the propeller is not suitable for the thrust range of PULSAR. This gives us 216 propellers in total. Then, for each small propeller, we choose a big propeller whose diameter is twice. For each pair of the big-small propeller, we evaluate the power of the big propeller at the thrust of PULSAR weight (i.e., 1234 g) and the power of the small

propeller at the thrust of 1/4 PULSAR weight (i.e., 308.5 g). Then, the power and thrust of the small propeller are multiplied by four so that the calculated total power and efficiency can be compared with the big propeller directly. Moreover, since momentum theory indicates an upper limit of the achievable performance neglecting all practical factors, such as propeller airfoil, pitch angle, loading distribution, etc., for each propeller size, we use the best propeller (i.e., the one with the lowest power and highest efficiency) to compare. The results are shown in Fig. S6. As can be seen, regardless of the propeller size, one big propeller has a consistently higher efficiency (in the range of 5.79% – 13.61%) than four small propellers when they have the same total disk area and thrust. The result is different from the prediction by momentum theory, which indicates the same efficiency. This is because the small propellers operate at much lower Reynolds numbers than large propellers. The low Reynolds numbers of the propellers make their performances difficult to predict (*64*).

Comparison of the propulsion systems

This section compares the efficiency of the propulsion system actually used by the benchmarked quadrotors and PULSAR. Two propulsion systems are used for the quadrotors in comparison: SUNNYSKY V2806 KV650 with GAMFAN 7535 for the 7.5-inch propeller quadrotor and SUNNYSKY V2806 KV650 with GAMFAN 8040 for the 8-inch propeller quadrotor. We compare the two quadrotors' propulsion systems with the propulsion system of PULSAR (i.e., T-MOTOR MN5006 KV450 motor and 14.8-inch T-MOTOR MF1302 blades with the swash-plateless mechanism).

We fix the three propulsion systems to the test stand and obtain the results shown in Fig. S7. As can be seen, the efficiency of PULSAR's propulsion system is 7.65 g/W while that of the quadrotors are 6.84 g/W (7.5-inch) and 8.07 g/W (8-inch). Although the 7.5-inch system has a similar (actually slightly larger) total disk area with PULSAR (1140.1 cm^2 versus 1110.4 cm^2), its efficiency is obviously lower (i.e., only 89.4% of PULSAR). The 10.6% efficiency difference is very close to the results obtained from the APC propeller database (which is about 7% on average as shown in Fig. S6). The slight mismatch is mainly caused by three reasons. The first reason is the mismatches between simulation and reality. The APC database are obtained by high-fidelity simulation, not real tests. The second reason is the differences in brand, propeller parameters, manufacturing quality, etc. Note that the 14.8-inch propeller of PULSAR and the 7.5-inch propeller of the quadrotor are neither APC propellers, nor even the same brand (for the sake of the highest possible efficiency in each its own size), their relative efficiencies are affected by propeller parameters, manufacturing quality, etc., hence are not the same 7% as for APC propellers. For the 8-inch system, although it has a much larger total disk area (1297.2 cm^2 versus 1110.4 cm^2), the efficiency only outperforms the PULSAR's 14.8-inch propeller slightly (i.e., 105.5% of PULSAR). The two results all show the superiority of the single-actuated system. The third reason is the differences in the motor loss. We calculate the motor copper loss according to the measured current and motor internal resistance (provided by the manufacturer), they are 3.71 W (14.8-inch), 3.40 W (7.5-inch), and 3.51 W (8-inch), respectively, which play very little role in the efficiency difference. However, other losses, such as iron loss, mechanical loss, and stray loss, cannot be measured and could contribute to the efficiency difference.

Comparison of the UAVs

This section compares the power and efficiency of the two quadrotors (one has 7.5-inch propellers, and the other has 8-inch propellers) with PULSAR. The test methods and results are shown in Fig. S8. For easy comparison, we also display the power consumed by only propulsion systems (from Fig. S7) in the same figure. As can be seen, from a standalone propulsion system to propulsion systems installed on airframes, PULSAR's mean efficiency drops 2.88% (from 7.65 g/W to 7.43 g/W), while quadrotor's efficiencies with 7.5-inch or 8-inch propellers drop 5.99% (from 6.84 g/W to 6.43 g/W) and 8.30% (from 8.07 g/W to 7.40 g/W), respectively. The resultant efficiencies of the quadrotors are merely 86.5% (7.5-inch propellers) or 99.6% (8-inch propellers) of PULSAR. Such efficiency drop from a standalone single propulsion system to on-airframe (multiple) propulsion systems can be mainly attributed to two reasons, the first one is the rotor-to-body interaction and the second one is the rotor-to-rotor interaction. The rotor-to-body interaction (or the effects of blockage) is that the UAV airframe located under the propeller(s) blocks a part of the high-speed downward airflow of the propeller(s), which causes a partial loss of the propeller thrust (*44*). This phenomenon happens in both PULSAR and the quadrotors, but the quadrotors have a more severe effect since the four arms are located under the propeller disk area that produces effective thrust, while the body of PULSAR is located under the propeller hub area that produces little thrust anyway. The rotor-to-rotor interaction is that the airflows from propellers interfere with each other, leading to thrust loss (or the same thrust but with more power) (*41–43*). These two reasons cause the efficiency of both quadrotors and PULSAR to drop, and moreover, cause the efficiency of quadrotors to drop more than PULSAR.

The increased number of propulsion systems on quadrotors contributes to more component weight than PULSAR when carrying the same payloads. Hence, we evaluate the efficiency when the quadrotors and PULSAR have to provide a thrust corresponding to their actual weight. As shown in Fig. S8C(ii), the quadrotor with 7.5-inch propellers has an efficiency of 6.15 g/W, which drops 4.35% from PULSAR's weight (from 6.43 g/W to 6.15 g/W), and the quadrotor with 8-inch propellers has an efficiency of 6.97 g/W, which drops 6.19% from PULSAR's weight (from 7.43 g/W to 6.97 g/W). PULSAR does not have this efficiency drop since it is evalated at its actual weight already.

Considering the power consumption of the onboard avionic systems, we measure the total power of the quadrotors and PULSAR in actual hover flights. When the UAVs are in real flights, due to the extra consumption of avionic devices (Table S4) and motor actuation, the mean efficiencies drop again for both quadrotors and PULSAR. The efficiency drop of PULSAR is 10.50% (7.43 g/W to 6.65 g/W), and that for the quadrotors are 7.97% (6.15 g/W to 5.66 g/W) for the 7.5-inch propeller quadrotor, and 8.32% (6.97 g/W to 6.39 g/W) for the 8-inch propeller quadrotor. The seemly higher efficiency drop of PULSAR when carrying the same payloads (which consumes the same power) is due to its smaller total power consumption.

Finally, considering all factors above, the overall power consumption of PULSAR is 26.7% less than the 7.5-inch propeller quadrotor (which has a similar propeller disk area) and 17.3% less than the 8-inch propeller quadrotor (which has a much larger propeller disk area), and the overall efficiency of PULSAR is 17.5% more than the 7.5-inch propeller quadrotor and 4.07%

more than the 8-inch propeller quadrotor.

Section S6. Comparison with commercial quadrotor UAVs

To further verify the efficiency of PULSAR, we compare it with common commercial quadrotor UAVs, including DJI Mavic Air 2, DJI Mavic 3, and DJI Phantom 4 Pro V2.0. In the specification provided by DJI, some UAVs (e.g., Mavic Air 2 and Mavic 3) have two time specs: one is the max hover time and the other is the max forward flight time (tested under 32.4 km/h flight speed). In our comparison, we use the hover time for both commercial quadrotors (read from the manufacturer's spec sheet) and PULSAR (measured from real hover flight tests).

To make a fair comparison between PULSAR and commercial UAVs, we first developed two variants of PULSAR in addition to the nominal design: the first one, denoted as "PULSAR (no LiDAR)", removes the LiDAR payload and the second one, denoted as "PULSAR (no LiDAR, 16.4″ propeller)", an additionally scales up the propeller to 16.4 inches (see Fig. S13). For the PULSAR (no LiDAR), additional structure is needed to hold the structure, leading to a total UAV weight of 750g. For PULSAR (no LiDAR, 16.4″ propeller), it has a larger propeller (16.4 inches versus the nominal 14.8 inches), and higher battery capacity (73.26 Wh versus the nominal 41.07 Wh). The total UAV weight is 929g.

The detailed parameters and results are shown in Table S1. In the table, the hover power of commercial UAVs is calculated from the battery energy and hover time both read from the manufacturer spec sheet. Similarly, the hover power of PULSAR is calculated from the voltage and current drained from the battery. In both cases, the hover power contains power consumption by all onboard electronics (although the number is very small when compared to the power on the propulsion system, see Table S4). The vehicle sizes of all UAVs include the sizes of propellers.

As shown in Table S1, first, we focus on PULSAR (no LiDAR) and DJI Mavic Air 2, because they have very similar battery energy (41.07 Wh versus 40.42 Wh) and total disk area (1110.4 cm^2 versus 1050.7 cm^2). Although PULSAR (no LiDAR) is considerably heavier than DJI Mavic Air 2 (750 g versus 570 g), which is disadvantageous to the efficiency (it has lower ideal efficiency according to momentum theory as shown in the last column of Table S1), it still achieves higher power efficiency than DJI Mavic Air 2 (8.20 g/W versus 7.76 g/W) in practice, showing the superiority of the single-actuated UAV. The larger weight of PULSAR (no LiDAR) causes higher hover power consumption (91.5 W versus 73.5 W), hence less flight time at a similar battery energy (26 min 26 s versus 33 min).

Second, we compare PULSAR (no LiDAR, 16.4″ propeller) with DJI Mavic 3. In this comparison, PULSAR (no LiDAR, 16.4″ propeller) has disadvantages in every aspect, including less battery energy (73.26 Wh versus 77 Wh), less total disk area (1362.8 cm^2 versus 1790.9 cm^2), and larger total weight (929 g versus 895 g). Despite these disadvantages of PULSAR (no LiDAR, 16.4″ propeller), which leads to a lower ideal efficiency (see the last column of Table S1), it achieves higher power efficiency (8.21 g/W versus 7.75 g/W) and slightly longer hover time (40 min 27 s versus 40 min) in practice, which supports the efficiency superiority of the single-actuated UAV again.

Third, we compare PULSAR (no LiDAR, 16.4″ propeller) with DJI Phantom 4 Pro V2.0. In this comparison, PULSAR (no LiDAR, 16.4″ propeller) has much less battery energy (73.26

Wh versus 89.2 Wh) and total disk area (1362.8 cm^2 versus 1790.9 cm^2), but is more lightweight (929 g versus 1375 g). In this case, PULSAR (no LiDAR, 16.4″ propeller) has slightly better efficiency in practice (8.21 g/W versus 7.71 g/W) and much longer hover time (40 min 27 s versus 30 min) even with an obviously lower battery energy. The results support the efficiency superiority of the single-actuated UAV further.

In all the above comparisons on efficiency, we would like to point out that, commercial quadrotor UAVs have highly optimized propulsion systems, including the propeller, motor, ESC, batteries, and even the body shape. In contrast, for PULSAR, we could only choose from a limited number of off-the-shelf propellers, motors, ESCs, and batteries without any optimization. For example, the batteries' energy densities for DJI Mavic Air 2 and DJI Mavic 3 are 0.204 Wh/g (40.42 Wh, 198 g) and 0.230 Wh/g (77 Wh, 335.5 g), respectively, while that of common LiPo battery used for PULSAR is 0.153 Wh/g (41.07 Wh, 268 g), which is only 75% of DJI Mavic Air 2 and 66.5% of DJI Mavic 3. The higher quality of components gives commercial UAVs in the above comparisons further more advantages. These advantages are partially cancelled by the additional power consumption of their onboard systems, including high-resolution camera, gimbal systems, operational video transmission systems, obstacle avoidance systems and onboard computers to process all this, which are not carried by the PULSAR variants. After accounting for all these, the higher flight efficiency achieved by PULSAR suggests a greater efficiency of the single-rotor configuration than quadrotor ones.

Finally, we look at the overall vehicle size. For the three DJI quadrotor UAVs we compared to, they always have larger sizes in both length and width than PULSAR, which limits their ability to fly in tighter spaces.

Section S7. Derivation of the simplified angular dynamics

Since the rotor part rotates in high speed, it can be deemed as a circular disk (call it rotor disk). Meanwhile, the origin of body frame $\mathcal{B}$ is located in the rotation axis of the rotor disk, so the rotor disk inertia $\mathbf{I}_R^{\mathcal{B}}$ seen in the body frame $\mathcal{B}$ is well approximated as a constant diagonal matrix where the first two diagonal elements are identical (i.e., $I_{R,x}^{\mathcal{B}} = I_{R,y}^{\mathcal{B}}$), leading to

$$\mathbf{I}_R^{\mathcal{B}} = \begin{bmatrix} I_{R,y}^B & 0 & 0 \\ 0 & I_{R,y}^B & 0 \\ 0 & 0 & I_{R,z}^B \end{bmatrix} \tag{S8}$$

Similarly, because of the approximately symmetric structure of both PULSAR's body and rotor disk, the whole UAV can also be deemed as symmetry. Hence, the inertia $\mathbf{I}_O^{\mathcal{B}}$ of the whole UAV seen in the body frame $\mathcal{B}$ is also a constant diagonal matrix with identical inertia in x and y directions (i.e., $I_{O,x}^{\mathcal{B}} = I_{O,y}^{\mathcal{B}}$), which is represented as

$$\mathbf{I}_O^{\mathcal{B}} = \begin{bmatrix} I_{O,y}^B & 0 & 0 \\ 0 & I_{O,y}^B & 0 \\ 0 & 0 & I_{O,z}^B \end{bmatrix} \tag{S9}$$

According to the angular dynamic model in Eq. 5

$$\mathbf{M}^{\mathcal{B}} = \lfloor \boldsymbol{\omega}^{\mathcal{B}} \rfloor (\mathbf{I}_O^{\mathcal{B}} \boldsymbol{\omega}^{\mathcal{B}} + \mathbf{I}_R^{\mathcal{B}} \boldsymbol{\Omega}^{\mathcal{B}}) + (\mathbf{I}_O^{\mathcal{B}} \dot{\boldsymbol{\omega}}^{\mathcal{B}} + \mathbf{I}_R^{\mathcal{B}} \dot{\boldsymbol{\Omega}}^{\mathcal{B}}) \tag{S10}$$

where $\boldsymbol{\omega}^{\mathcal{B}} = [\omega_x^{\mathcal{B}}, \omega_y^{\mathcal{B}}, \omega_z^{\mathcal{B}}]^T$ and $\boldsymbol{\Omega}^{\mathcal{B}} = [0, 0, \sigma]^T$ with σ being the rotor speed with respect to the stator, the first term can be further expressed as

$$\lfloor \boldsymbol{\omega}^{\mathcal{B}} \rfloor (\mathbf{I}_O^{\mathcal{B}} \boldsymbol{\omega}^{\mathcal{B}} + \mathbf{I}_R^{\mathcal{B}} \boldsymbol{\Omega}^{\mathcal{B}}) = \begin{bmatrix} \omega_x^{\mathcal{B}} \\ \omega_y^{\mathcal{B}} \\ \omega_z^{\mathcal{B}} \end{bmatrix} \times \begin{bmatrix} I_{O,y}^B \omega_x^{\mathcal{B}} \\ I_{O,y}^B \omega_y^{\mathcal{B}} \\ I_{O,z}^B \omega_z^{\mathcal{B}} + I_{R,z}^B \sigma \end{bmatrix} = \begin{bmatrix} (I_{O,z}^B - I_{O,y}^B) \omega_y^{\mathcal{B}} \omega_z^{\mathcal{B}} + I_{R,z}^B \omega_y \sigma \\ -(I_{O,z}^B - I_{O,y}^B) \omega_x^{\mathcal{B}} \omega_z^{\mathcal{B}} - I_{R,z}^B \omega_x \sigma \\ 0 \end{bmatrix} \tag{S11}$$

Define $\mathbf{L}_{\text{gyro}}^{\mathcal{B}}$ as

$$\mathbf{L}_{\text{gyro}}^{\mathcal{B}} = \begin{bmatrix} 0 \\ 0 \\ (I_{O,z}^{\mathcal{B}} - I_{O,y}^{\mathcal{B}}) \omega_z^{\mathcal{B}} + I_{R,z}^{\mathcal{B}} \sigma \end{bmatrix} \tag{S12}$$

Then we can obtain

$$\begin{aligned} -\lfloor \mathbf{L}_{\text{gyro}}^{\mathcal{B}} \rfloor \boldsymbol{\omega}_{xy}^{\mathcal{B}} = \lfloor \boldsymbol{\omega}_{xy}^{\mathcal{B}} \rfloor \mathbf{L}_{\text{gyro}}^{\mathcal{B}} &= \begin{bmatrix} \omega_x^{\mathcal{B}} \\ \omega_y^{\mathcal{B}} \\ 0 \end{bmatrix} \times \begin{bmatrix} 0 \\ 0 \\ (I_{O,z}^{\mathcal{B}} - I_{O,y}^{\mathcal{B}}) \omega_z^{\mathcal{B}} + I_{R,z}^{\mathcal{B}} \sigma \end{bmatrix} \\ &= \begin{bmatrix} (I_{O,z}^B - I_{O,y}^B) \omega_y^{\mathcal{B}} \omega_z^{\mathcal{B}} + I_{R,z}^B \omega_y \sigma \\ -(I_{O,z}^B - I_{O,y}^B) \omega_x^{\mathcal{B}} \omega_z^{\mathcal{B}} - I_{R,z}^B \omega_x \sigma \\ 0 \end{bmatrix} = \lfloor \boldsymbol{\omega}^{\mathcal{B}} \rfloor (\mathbf{I}_O^{\mathcal{B}} \boldsymbol{\omega}^{\mathcal{B}} + \mathbf{I}_R^{\mathcal{B}} \boldsymbol{\Omega}^{\mathcal{B}}) \end{aligned} \tag{S13}$$

For the second term of Eq. S10, it can be further expressed as

$$\mathbf{I}_O^{\mathcal{B}} \dot{\boldsymbol{\omega}}^{\mathcal{B}} + \mathbf{I}_R^{\mathcal{B}} \dot{\boldsymbol{\Omega}}^{\mathcal{B}} = \begin{bmatrix} I_{O,y}^B \dot{\omega}_x^{\mathcal{B}} \\ I_{O,y}^B \dot{\omega}_y^{\mathcal{B}} \\ I_{O,z}^B \dot{\omega}_z^{\mathcal{B}} + I_{R,z}^B \dot{\sigma} \end{bmatrix} = \underbrace{\begin{bmatrix} I_{O,y}^B \dot{\omega}_x^{\mathcal{B}} \\ I_{O,y}^B \dot{\omega}_y^{\mathcal{B}} \\ 0 \end{bmatrix}}_{\mathbf{I}_O^{\mathcal{B}} \dot{\boldsymbol{\omega}}_{xy}^{\mathcal{B}}} + \begin{bmatrix} 0 \\ 0 \\ I_{O,z}^B \dot{\omega}_z^{\mathcal{B}} + I_{R,z}^B \dot{\sigma} \end{bmatrix} \tag{S14}$$

From Eq. S11 and Eq. S14, the right hand side of Eq. S10 is

$$\begin{aligned} &\lfloor \boldsymbol{\omega}^{\mathcal{B}} \rfloor (\mathbf{I}_O^{\mathcal{B}} \boldsymbol{\omega}^{\mathcal{B}} + \mathbf{I}_R^{\mathcal{B}} \boldsymbol{\Omega}^{\mathcal{B}}) + (\mathbf{I}_O^{\mathcal{B}} \dot{\boldsymbol{\omega}}^{\mathcal{B}} + \mathbf{I}_R^{\mathcal{B}} \dot{\boldsymbol{\Omega}}^{\mathcal{B}}) \\ &= \underbrace{\begin{bmatrix} (I_{O,z}^B - I_{O,y}^B) \omega_y^{\mathcal{B}} \omega_z^{\mathcal{B}} + I_{R,z}^B \omega_y \sigma \\ -(I_{O,z}^B - I_{O,y}^B) \omega_x^{\mathcal{B}} \omega_z^{\mathcal{B}} - I_{R,z}^B \omega_x \sigma \\ 0 \end{bmatrix}}_{-\lfloor \mathbf{L}_{\text{gyro}}^{\mathcal{B}} \rfloor \boldsymbol{\omega}_{xy}^{\mathcal{B}} \text{ from Eq. S13}} + \underbrace{\begin{bmatrix} I_{O,y}^B \dot{\omega}_x^{\mathcal{B}} \\ I_{O,y}^B \dot{\omega}_y^{\mathcal{B}} \\ 0 \end{bmatrix}}_{\mathbf{I}_O^{\mathcal{B}} \dot{\boldsymbol{\omega}}_{xy}^{\mathcal{B}}} + \begin{bmatrix} 0 \\ 0 \\ I_{O,z}^B \dot{\omega}_z^{\mathcal{B}} + I_{R,z}^B \dot{\sigma} \end{bmatrix} \end{aligned} \tag{S15}$$

Furthermore, the left hand side of Eq. S10 is

$$\mathbf{M}^{\mathcal{B}} = \begin{bmatrix} M_x^{\mathcal{B}} \\ M_y^{\mathcal{B}} \\ M_{\text{prop}}^{\mathcal{B}} + M_{\text{body}}^{\mathcal{B}} \end{bmatrix} = \underbrace{\begin{bmatrix} M_x^{\mathcal{B}} \\ M_y^{\mathcal{B}} \\ 0 \end{bmatrix}}_{\mathbf{M}_{xy}^{\mathcal{B}}} + \begin{bmatrix} 0 \\ 0 \\ M_{\text{prop}}^{\mathcal{B}} + M_{\text{body}}^{\mathcal{B}} \end{bmatrix} \tag{S16}$$

Therefore, separating the dynamics in x-y plane from that along the z axis in Eq. S10 implies

$$\mathbf{M}_{xy}^{\mathcal{B}} = \mathbf{I}_O^{\mathcal{B}} \dot{\boldsymbol{\omega}}_{xy}^{\mathcal{B}} - \lfloor \mathbf{L}_{\text{gyro}}^{\mathcal{B}} \rfloor \boldsymbol{\omega}_{xy}^{\mathcal{B}} \tag{S17}$$

and

$$M^{\mathcal{B}}_{\text{prop}} + M^{\mathcal{B}}_{\text{body}} = I^{B}_{O,z}\dot{\omega}^{\mathcal{B}}_{z} + I^{B}_{R,z}\dot{\sigma} \tag{S18}$$

Since PULSAR is designed to rotate freely along its body z-axis, so the rotation dynamics about z-axis in Eq. S18 is not concerned and only the rotation dynamics along the x- and y-axis in Eq. S17 matters, which is the Eq. 7 in the main text.

Section S8. Derivation of the rotation kinematics

The kinematics of $\mathbf{z}^{\mathcal{I}}_{\mathcal{B}}$ represented in the inertia frame is

$$\dot{\mathbf{z}}^{\mathcal{I}}_{\mathcal{B}} = \boldsymbol{\omega}^{\mathcal{I}} \times \mathbf{z}^{\mathcal{I}}_{\mathcal{B}} \tag{S19}$$

Transforming the angular velocity $\boldsymbol{\omega}^{\mathcal{I}}$ to body frame, yielding

$$\dot{\mathbf{z}}^{\mathcal{I}}_{\mathcal{B}} = \lfloor \mathbf{R}^{\mathcal{I}\mathcal{B}}\boldsymbol{\omega}^{\mathcal{B}} \rfloor \mathbf{z}^{\mathcal{I}}_{\mathcal{B}} = \mathbf{R}^{\mathcal{I}\mathcal{B}} \lfloor \boldsymbol{\omega}^{\mathcal{B}} \rfloor \mathbf{z}^{\mathcal{B}}_{\mathcal{B}} = \mathbf{R}^{\mathcal{I}\mathcal{B}} \lfloor \boldsymbol{\omega}^{\mathcal{B}} \rfloor \mathbf{e}_3 \tag{S20}$$

where $\mathbf{e}_3 = [0, 0, 1]^T$. Since $\lfloor \boldsymbol{\omega}^{\mathcal{B}} \rfloor \mathbf{e}_3 = \lfloor \boldsymbol{\omega}^{\mathcal{B}}_{xy} \rfloor \mathbf{e}_3$,

$$\dot{\mathbf{z}}^{\mathcal{I}}_{\mathcal{B}} = \mathbf{R}^{\mathcal{I}\mathcal{B}} \lfloor \boldsymbol{\omega}^{\mathcal{B}}_{xy} \rfloor \mathbf{e}_3 = \mathbf{R}^{\mathcal{I}\mathcal{B}} \lfloor \boldsymbol{\omega}^{\mathcal{B}}_{xy} \rfloor \mathbf{z}^{\mathcal{B}}_{\mathcal{B}} = \boldsymbol{\omega}^{\mathcal{I}}_{xy} \times \mathbf{z}^{\mathcal{I}}_{\mathcal{B}}. \tag{S21}$$

Section S9. Convergence proof of attitude control

Define Lyapunov function

$$V(\xi) = 1 - \cos(\xi) = 1 - \mathbf{z}^{\mathcal{I}}_{\mathcal{B},d} \cdot \mathbf{z}^{\mathcal{I}}_{\mathcal{B}} \tag{S22}$$

where $\xi \in (-\pi, \pi]$ is the intersection angle between $\mathbf{z}^{\mathcal{I}}_{\mathcal{B},d}$ and $\mathbf{z}^{\mathcal{I}}_{\mathcal{B}}$. Assuming the desired attitude $\mathbf{z}^{\mathcal{I}}_{\mathcal{B},d}$ is a constant vector, then

$$\dot{V}(\xi) = -\mathbf{z}^{\mathcal{I}}_{\mathcal{B},d} \cdot \dot{\mathbf{z}}^{\mathcal{I}}_{\mathcal{B}} \tag{S23}$$

According to the attitude kinematics, we obtain

$$\dot{V}(\xi) = -\mathbf{z}^{\mathcal{I}}_{\mathcal{B},d} \cdot \left(\boldsymbol{\omega}^{\mathcal{I}}_{xy} \times \mathbf{z}^{\mathcal{I}}_{\mathcal{B}}\right) \tag{S24}$$

Assuming the angular velocity is accurately tracked $\boldsymbol{\omega}^{\mathcal{I}}_{xy} = \boldsymbol{\omega}^{\mathcal{I}}_{xy,d}$ and substituting the attitude controller law $\boldsymbol{\omega}^{\mathcal{I}}_{xy,d} = k^a_p(\mathbf{z}^{\mathcal{I}}_{\mathcal{B}} \times \mathbf{z}^{\mathcal{I}}_{\mathcal{B},d})$,

$$\begin{aligned}
\dot{V}(\xi) &= -k^a_p \mathbf{z}^{\mathcal{I}}_{\mathcal{B},d} \cdot \left(\left(\mathbf{z}^{\mathcal{I}}_{\mathcal{B}} \times \mathbf{z}^{\mathcal{I}}_{\mathcal{B},d}\right) \times \mathbf{z}^{\mathcal{I}}_{\mathcal{B}}\right) \\
&= -k^a_p \mathbf{z}^{\mathcal{I}}_{\mathcal{B},d} \cdot \left(-\left(\mathbf{z}^{\mathcal{I}}_{\mathcal{B}} \cdot \mathbf{z}^{\mathcal{I}}_{\mathcal{B},d}\right) \cdot \mathbf{z}^{\mathcal{I}}_{\mathcal{B}} + \left(\mathbf{z}^{\mathcal{I}}_{\mathcal{B}} \cdot \mathbf{z}^{\mathcal{I}}_{\mathcal{B}}\right) \cdot \mathbf{z}^{\mathcal{I}}_{\mathcal{B},d}\right) \\
&= -k^a_p \left(-\left(\mathbf{z}^{\mathcal{I}}_{\mathcal{B},d} \cdot \mathbf{z}^{\mathcal{I}}_{\mathcal{B}}\right)^2 + 1\right) \\
&= -k^a_p \left(1 - \cos^2(\xi)\right) \\
&= -k^a_p \sin^2(\xi) < 0, \forall \xi \in (-\pi, 0) \cup (0, \pi)
\end{aligned} \tag{S25}$$

which means that $V(\xi)$ (hence ξ) monotonically decreasing until reaching $\xi = 0$ for any $\xi \in (-\pi, \pi)$. Hence, the $\mathbf{z}^{\mathcal{I}}_{\mathcal{B}}$ converges to $\mathbf{z}^{\mathcal{I}}_{\mathcal{B},d}$ as long as their initial intersection angle ξ does not reach π (i.e., $\mathbf{z}^{\mathcal{I}}_{\mathcal{B}} \neq -\mathbf{z}^{\mathcal{I}}_{\mathcal{B},d}$).

Section S10. Description of the extended Kalman filter

The extended Kalman filter (EKF) used in PULSAR is provided by the PX4 firmware (i.e., ECL EKF2 module), which contains the state vector $\mathbf{x}$ as

$$\mathbf{x} = [\mathbf{q}, \mathbf{v}^{\mathcal{I}}, \mathbf{p}^{\mathcal{I}}, \mathbf{b}_{\omega}^{\mathcal{B}}, \mathbf{b}_{a}^{\mathcal{B}}, \mathbf{m}^{\mathcal{I}}, \mathbf{b}_{m}^{\mathcal{B}}, \mathbf{v}_{w}^{\mathcal{I}}]^{T} \tag{S26}$$

where the order is same as the realization in PX4, $\mathbf{q}$ is the quaternion represented the attitude of body frame $\mathcal{B}$ with respect to the inertial frame $\mathcal{I}$, $\mathbf{v}^{\mathcal{I}}$, $\mathbf{p}^{\mathcal{I}}$, and $\mathbf{m}^{\mathcal{I}}$ are the velocity, position, and earth magnetic field vector, respectively, and they are all represented in the inertial frame $\mathcal{I}$. $\mathbf{b}_{\omega}^{\mathcal{B}}$, $\mathbf{b}_{a}^{\mathcal{B}}$, and $\mathbf{b}_{m}^{\mathcal{B}}$ are the bias of gyroscope, accelerometer, and magnetometer, respectively, and they are all represented in the body frame $\mathcal{B}$. $\mathbf{v}_{w}^{\mathcal{I}}$ is a 2D wind velocity vector perpendicular to the z-axis of the intertial frame $\mathbf{z}_{\mathcal{I}}$.

Many sensors can be fused by the EKF on PX4 firmware, such as inertial measurement unit (IMU), global positioning system (GPS), magnetometer, barometer, airspeed head, and external observation system providing position and attitude measurements. To estimate the fast z-axis rotation of PULSAR, we use a LiDAR-inertial odometry (LIO) system, FAST-LIO2 (*56*), to obtain a high-quality estimation of the full state including the position, velocity, and attitude of PULSAR. Then, the attitude and position estimated by FAST-LIO2 are sent to the EKF as the external observation by using MAVROS (*55*). The EKF outputs a 200-Hz attitude, a much higher rate than the attitude estimation frequency of FAST-LIO2 (i.e., 50 Hz), to satisfy the requirement of the 200-Hz attitude controller.

To cope with the fast self-rotation, we need to tune the parameters of the EKF, including sensor noise and sensor delay. One crucial parameter is the sensor delay parameter τ, which indicates the delay from the time when the sensor measurements are sampled to the time the measurements are received by the EKF. Once receiving the sensor measurement, the EKF would compensate the measurements delay by updating the state that is $[\tau/\Delta t]$ steps in the past, with Δt being the state discretization period, and re-predicting all the subsequent state until the current step. It is important that the delay parameter of each sensor is specified correctly. If the specified delay is too far from the actual sensor delay, the EKF will update the states at wrong steps, which, when coupled with the fast self-rotation, would cause the state estimate to diverge. In our tests, the delay time of the LIO system is about 40 ms. We also set the delay time of other sensors not in use (e.g., GPS, range sensor, airspeed head, etc.) to zeros in order to avoid any side effect.

Section S11. Implementation of the attitude controller

There are mainly three control modules in PX4 firmware: the position & velocity control module, the attitude control module, and the angular velocity control module. They run separately with different frequencies and their connections are based on the micro object request broker (uORB) topics. Our attitude controller is embedded into the attitude control module by modifying the source code.

The attitude controller is summarized in Algorithm 1. The position & velocity control module generates the desired attitude $\mathbf{z}_{\mathcal{B},d}^{\mathcal{I}}$ in the inertial frame and publishes it to the uORB topic. Meanwhile, the current attitude of the UAV is continuously estimated by the EKF and published

to the uORB topic as well. Then, if the attitude controller receives a new sample of the 200-Hz current attitude, the newest 50-Hz $\mathbf{z}_{\mathcal{B},d}^{\mathcal{I}}$ is read out, and they are used to calculate the desired angular velocity $\boldsymbol{\omega}_{xy,d}^{\mathcal{I}}$, which is represented in the inertial frame $\mathcal{I}$. Using the current attitude again, the desired angular velocity $\boldsymbol{\omega}_{xy,d}^{\mathcal{I}}$ can be transformed to the body frame and the result $\boldsymbol{\omega}_{xy,d}^{\mathcal{B}}$ is published to the uORB topic for the tracking of the angular velocity controller.

Algorithm 1: Attitude Controller

Input : Desired attitude in inertial frame $\mathbf{z}_{\mathcal{B},d}^{\mathcal{I}}$, current attitude $\mathbf{R}^{\mathcal{IB}}$
Output : Desired angular velocity in body frame $\boldsymbol{\omega}_{xy,d}^{\mathcal{B}}$
Variable : Desired angular velocity in inertial frame $\boldsymbol{\omega}_{xy,d}^{\mathcal{I}}$
Parameter: Proportional gain of the attitude controller k_p^a

while *True* **do**
  if $\mathbf{R}^{\mathcal{IB}}$ *is updated* **then**
    $\mathbf{z}_{\mathcal{B}}^{\mathcal{I}} \leftarrow \mathbf{R}^{\mathcal{IB}}\mathbf{z}_{\mathcal{B}}^{\mathcal{B}}$
    $\boldsymbol{\omega}_{xy,d}^{\mathcal{I}} \leftarrow k_p^a \left(\mathbf{z}_{\mathcal{B}}^{\mathcal{I}} \times \mathbf{z}_{\mathcal{B},d}^{\mathcal{I}}\right)$ (Eq. 12)
    $\boldsymbol{\omega}_{xy,d}^{\mathcal{B}} \leftarrow \left(\mathbf{R}^{\mathcal{IB}}\right)^T \boldsymbol{\omega}_{xy,d}^{\mathcal{I}}$ (Eq. 13)
    Publish($\boldsymbol{\omega}_{xy,d}^{\mathcal{B}}$);
  end
end

Section S12. Captions of Supplementary Movies

Movie S1. Cyclic pitch angle changes of the swashplateless mechanism.
Movie S2. Hover time test.
Movie S3. Trajectory tracking in indoor environment.
Movie S4. Response to position commands.
Movie S5. Robustness to external disturbances.
Movie S6. Autonomous navigation in unknown, GNSS-denied environments.
Movie S7. Cave mapping application.
Movie S8. Avoidance of dynamic obstacles from different directions.
Movie S9. Hover time test of PULSAR (no LiDAR).
Movie S10. Hover time test of PULSAR (no LiDAR, 16.4-inch propeller).

Supplementary Figures and Tables

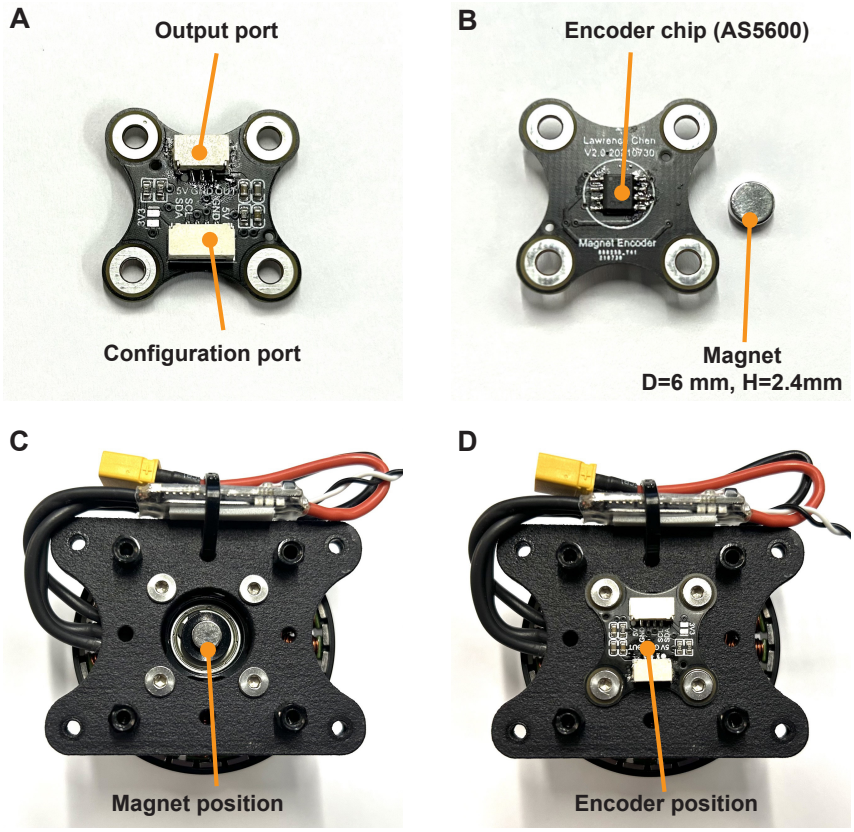

Fig. S1. The hardware and installation of the magnetic encoder. (**A**) The upward side. (**B**) The downward side and the magnet whose diameter and height are 6 mm and 2.4 mm, respectively. (**C**) The installation position of the magnet. (**D**) The installation position of the magnetic encoder board.

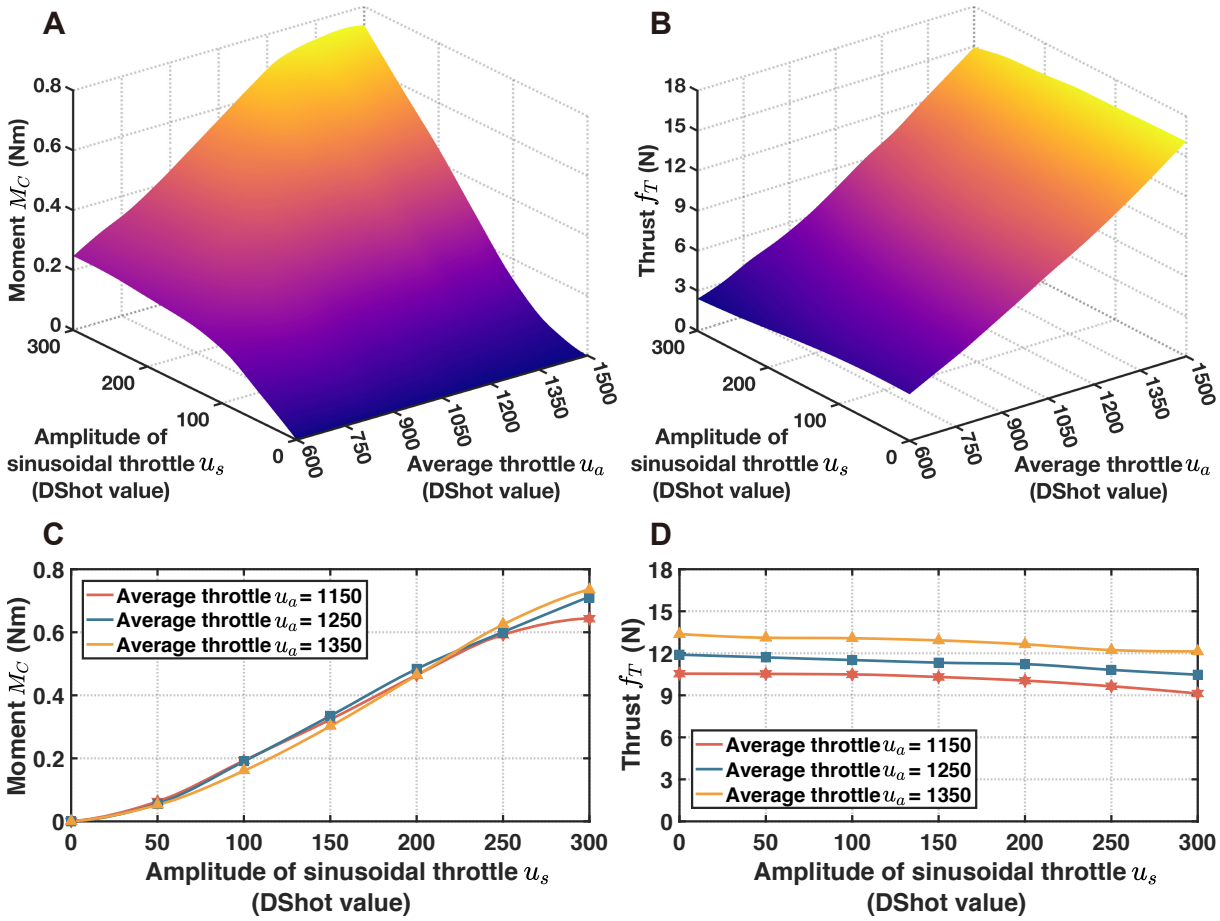

Fig. S2. Characteristics of moment and thrust of the swashplateless mechanism. (**A**) The moment magnitude M_C versus the amplitude of sinusoidal throttle u_s and the average throttle u_a. (**B**) The thrust f_T versus the amplitude of sinusoidal throttle u_s and the average throttle u_a. In figures (A) and (B), the u_a and u_s are represented by the DShot value (defined by the DShot protocol) which has a range from 0 to 2047. (**C**) The relation between moment magnitude M_C and sinusoidal amplitude u_s around the hovering throttle (i.e., $u_a = 1250$ in DShot value). (**D**) The relation between thrust f_T and sinusoidal amplitude u_s around the hovering throttle (i.e., $u_a = 1250$ in DShot value).

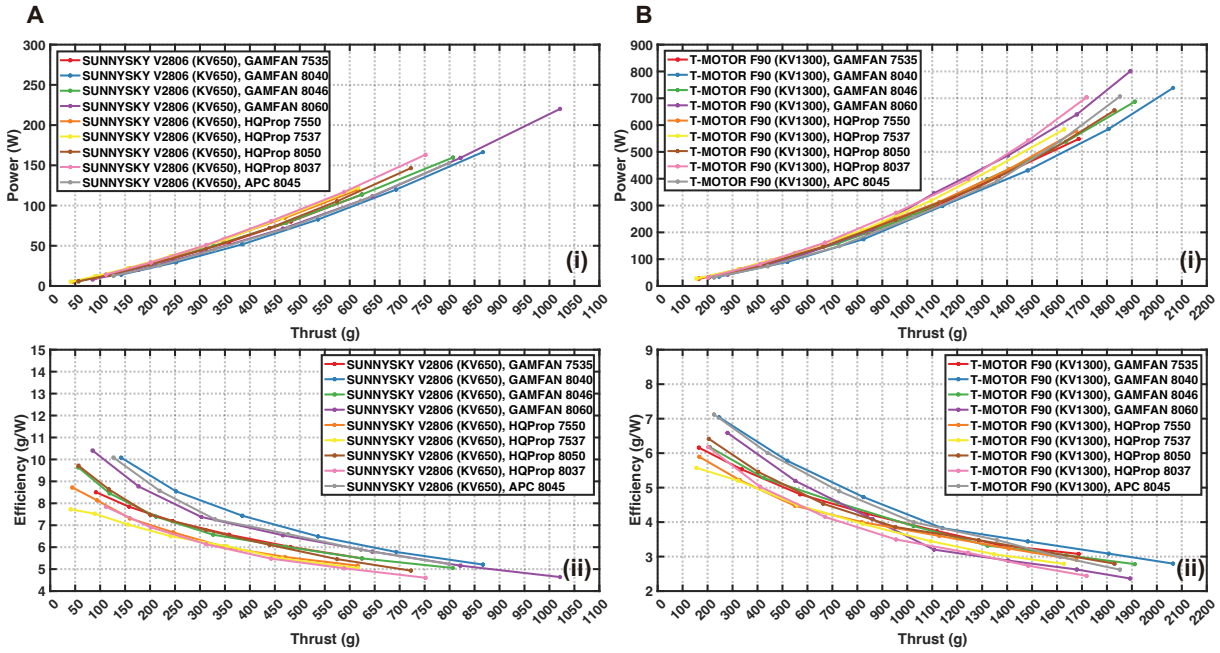

Fig. S3. The performance comparison of propellers. Power and efficiency of nine candidate propellers with motor SUNNYSKY V2806 KV650 (Left) and motor T-MOTOR F90 KV1300 (Right).

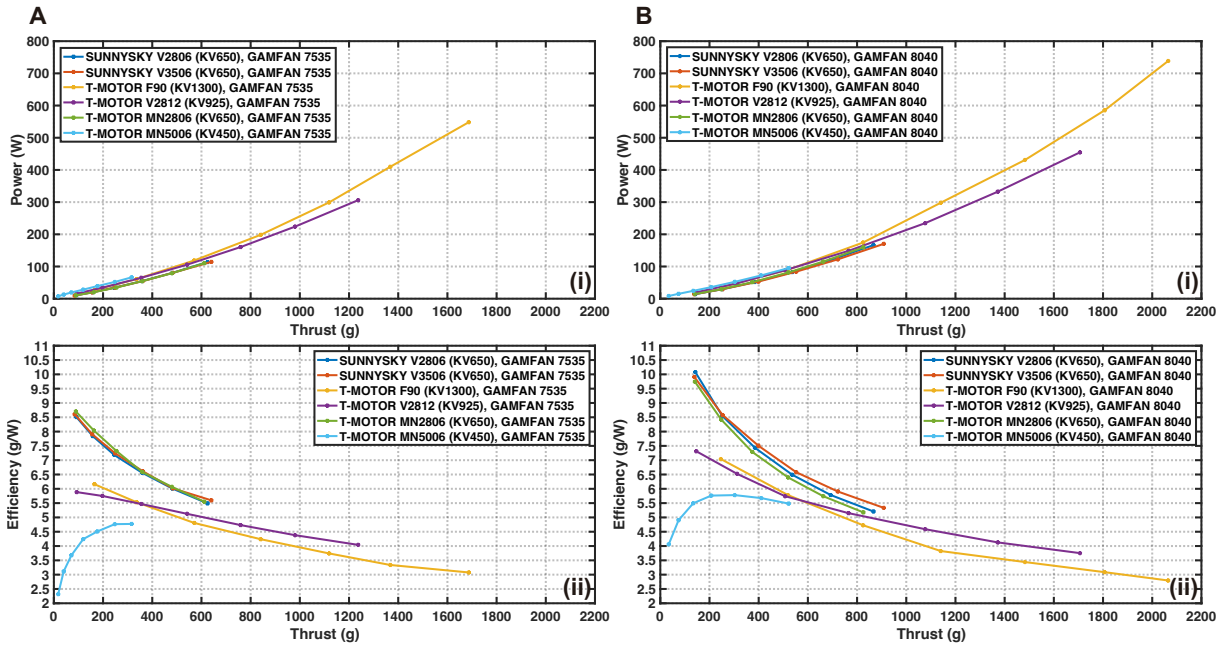

Fig. S4. The performance comparison of motors. Power and efficiency of six candidate motors with propeller GAMFAN 7535 (Left) and GAMFAN 8040 (Right).

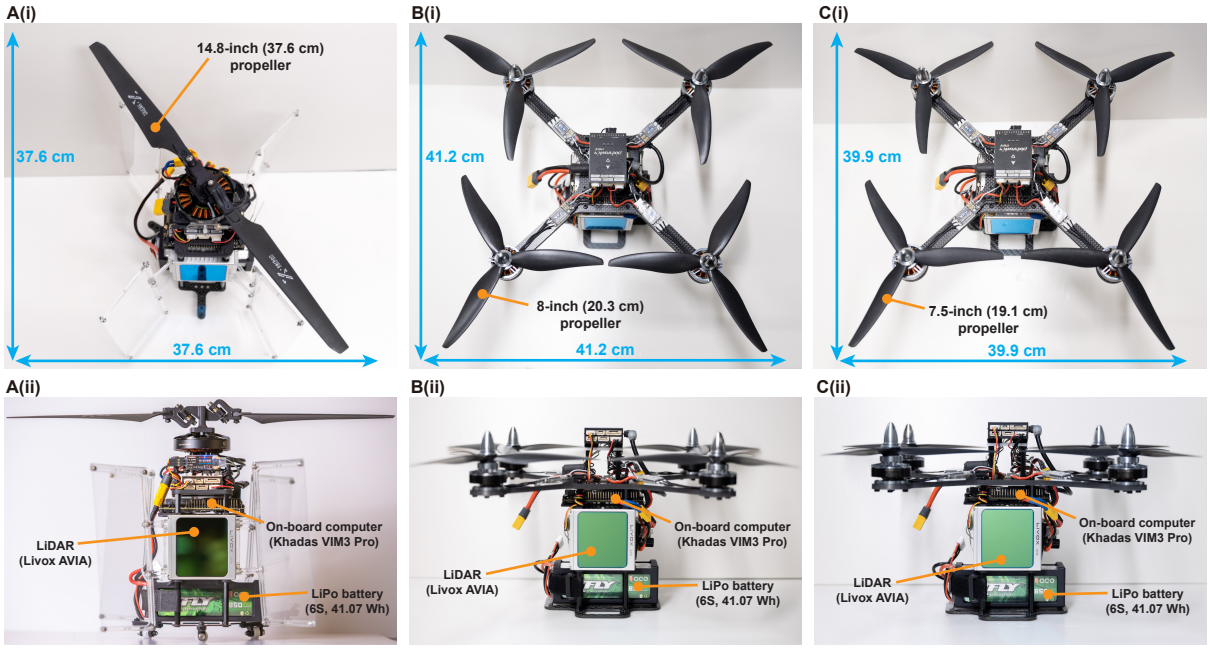

Fig. S5. The benchmarked quadrotors with the same payloads and similar total propeller disk area used for comparison study. The length and width include the size of propellers. (**A**) PULSAR. (**B**) The benchmarked quadrotor with 8-inch propellers. (**C**) The benchmarked quadrotor with 7.5-inch propellers.

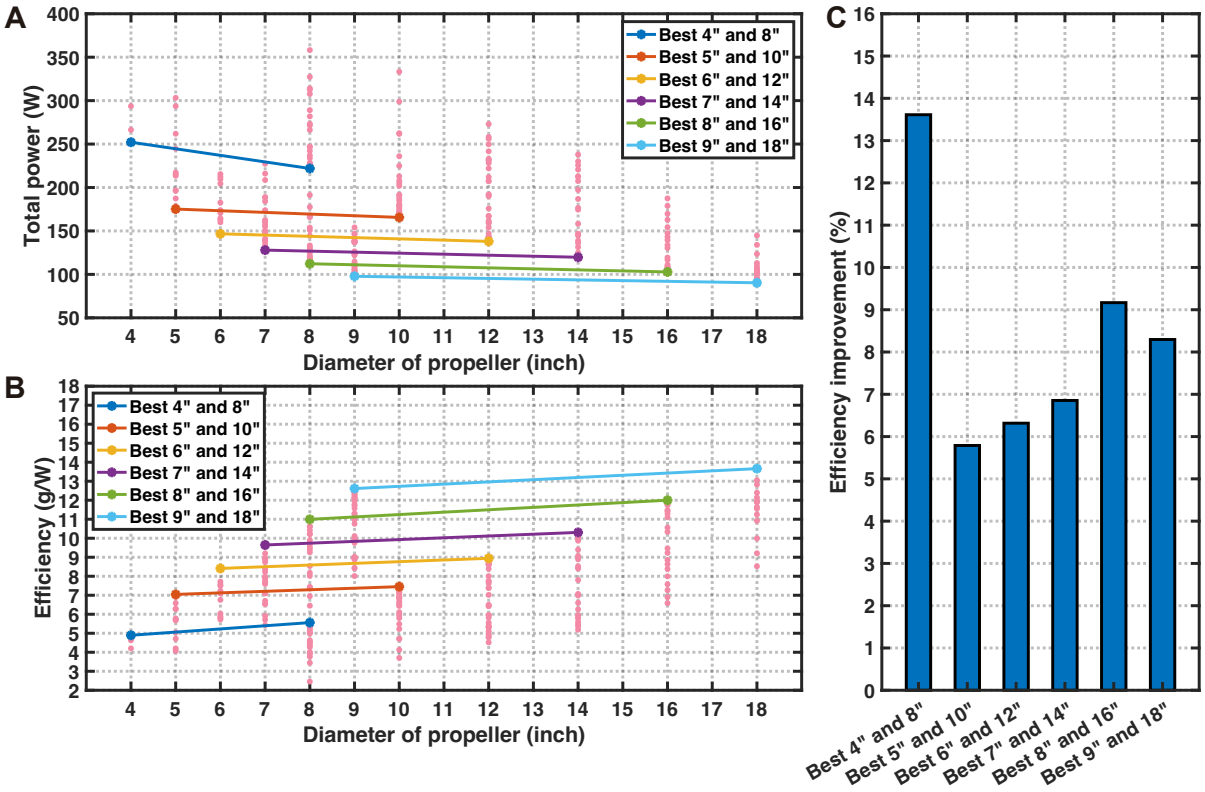

Fig. S6. Power and efficiency comparison based on APC's propeller database. Power and efficiency comparison between one big propeller and four smaller propellers with the same disk area and thrust. 216 propeller are used in total and each pink point represents the data of one propeller. For each pair of big-small propeller, the best propeller in each size is used in the comparison. (**A**) Total power comparison. (**B**) Efficiency comparison. (**C**) Efficiency improvement of one big propeller over four small propellers.

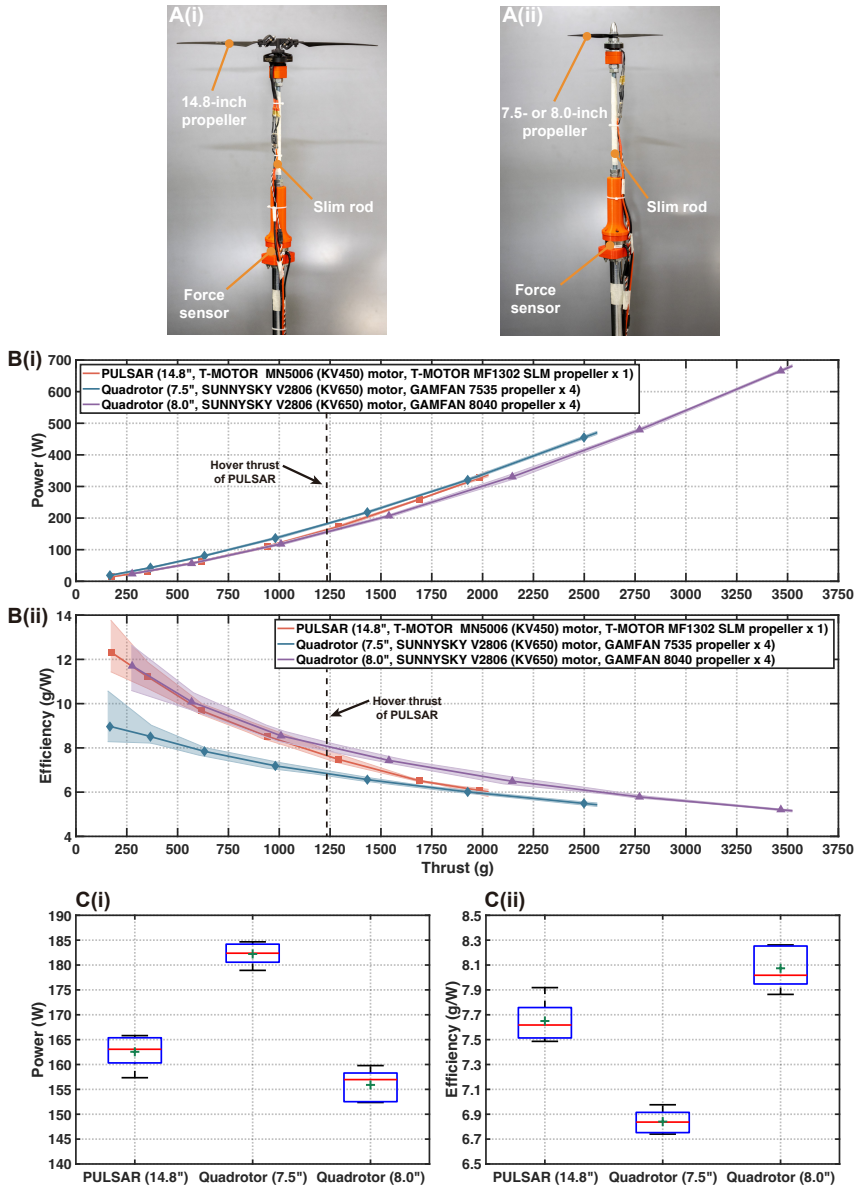

Fig. S7. Propulsion system comparison of PULSAR (14.8-inch propeller) and the quadrotors (7.5-inch and 8-inch propellers). (**A**) Test stand for PULSAR and quadrotors. To avoid the influence of ground effect or possible airflow blockage affecting the propeller efficiency, the propeller is installed at the top of a slim rod. (**B**) The power-thrust and efficiency-thrust curves of the three propulsion systems. The SLM in the legend is an acronym of the swashplateless mechanism. For quadrotors, the thrust and power are multiplied by four to make a direct comparison with PULSAR. Each propulsion is tested for five times with their error bands shown as the shaded area. For the efficiency, the value at low thrust region has larger error bands due to the very small power consumption on the denominator of the efficiency calculation, so a small error in power measurement would cause large change in the efficiency. (**C**) The power and efficiency of the three propulsion systems when providing the hover thrust for PULSAR (i.e., 1234 g). The green marker "+" denotes the mean value. The red lines in the center of the box indicate the median values, the top and bottom edge of the box indicate the 25th and 75th percentile, respectively. The top and bottom lines above and below the box represent the maximum and minimum values, respectively.

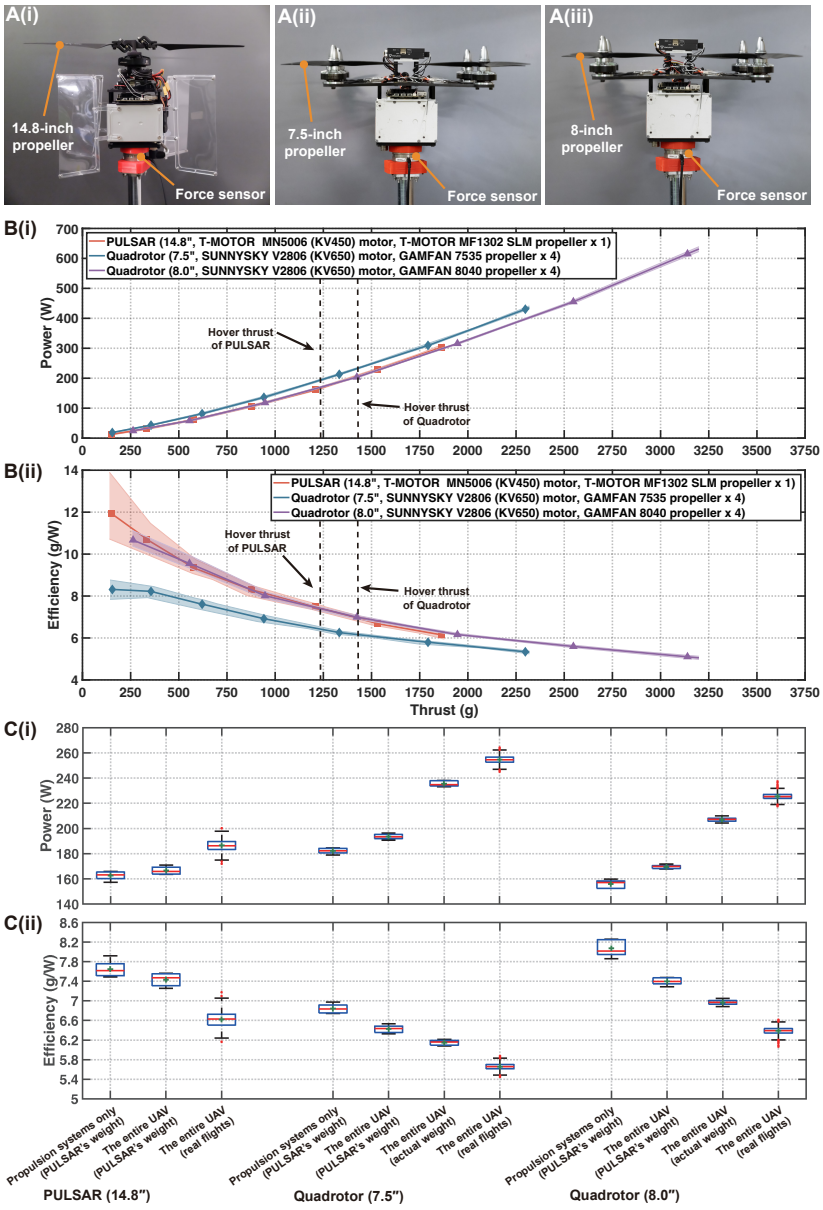

Fig. S8. Comparison between PULSAR and the two quadrotors. (**A**) Test stand for PULSAR and quadrotors. (**B**) The power-thrust and efficiency-thrust curves of the three UAVs. The SLM in the legend is an acronym of the swashplateless mechanism. Each UAV is tested for five times with their error bands shown as the shaded area. For the efficiency, the value at low thrust region has larger error bands due to the very small power consumption on the denominator of the efficiency calculation, so a small error in power measurement would cause large change in the efficiency. (**C**) The power and efficiency of the propulsion systems only (with the weight of PULSAR), the entire UAV (with the weight of PULSAR), the entire UAV (with the UAV actual weight), and the entire UAV (in real flights) of quadrotors and PULSAR. The power and efficiency of the propulsion systems are drawn from Fig. S7 directly, and that of the entire UAV (in real flights) are the total power consumption (including avionic devices) measured in actual hover flights. The red lines inside the box indicate the median values, the green "+" markers indicate the mean values, the top and bottom edge of the box indicate the 25th and 75th percentile, respectively. The top and bottom lines above and below the box represent the maximum and minimum values, respectively. The outliers are represented as red points.

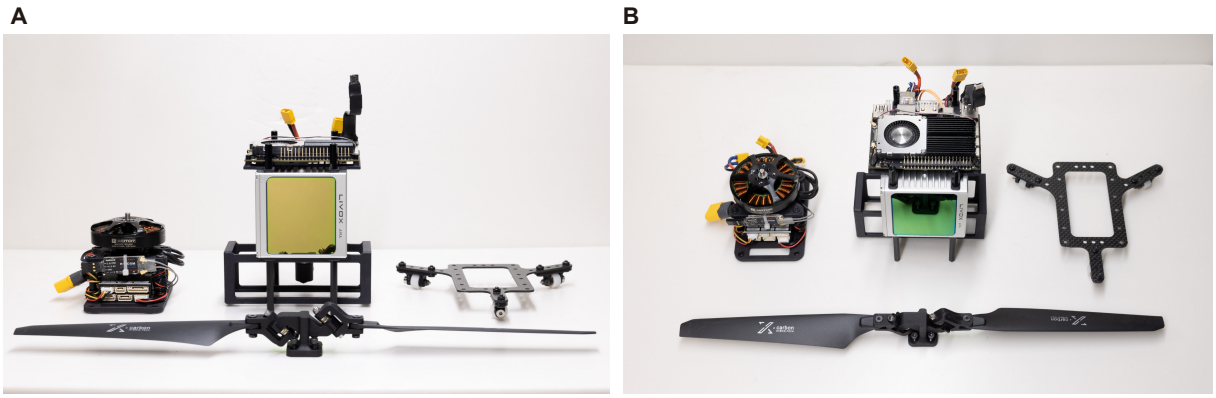

Fig. S9. The divided parts of PULSAR. (**A**) Front view. (**B**) Top view.

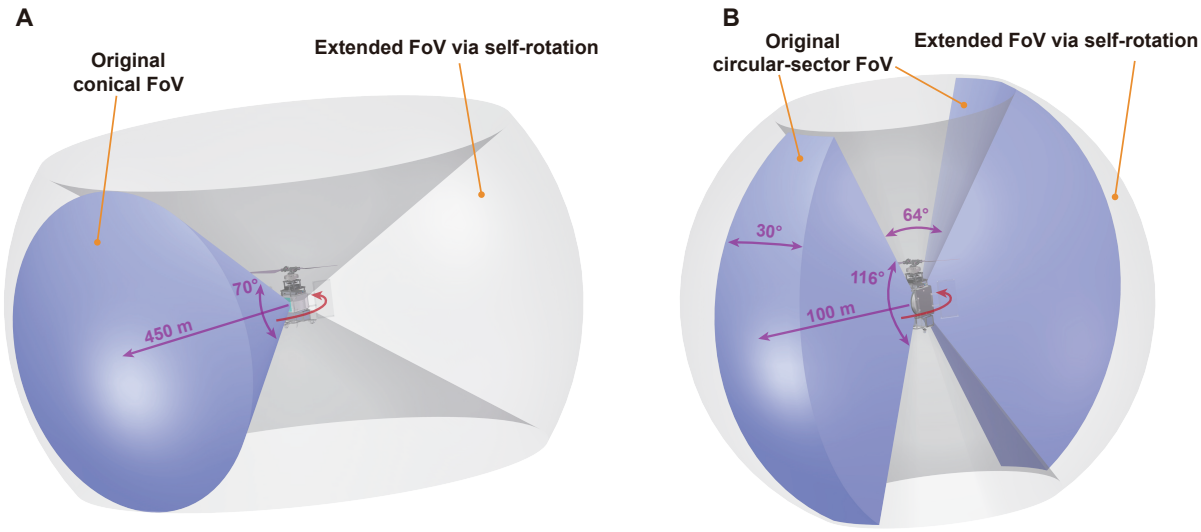

Fig. S10. Comparison between sensor original FoV and the extended FoV via self-rotation of PULSAR. The blue area represents the original FoV while the grey area represents the extended FoV. (**A**) Conical FoV LiDAR (e.g., Livox AVIA). The original FoV has a solid angle of 1.40 sr while the extended FoV has a solid angle of 7.21 sr. (**B**) 360-degree-FoV LiDAR (e.g., Velodyne Puck LITE). The original FoV has a solid angle of 3.25 sr while the extended FoV has a solid angle of 10.66 sr. The area occluded by the UAV structure on the top and bottom has been excluded.

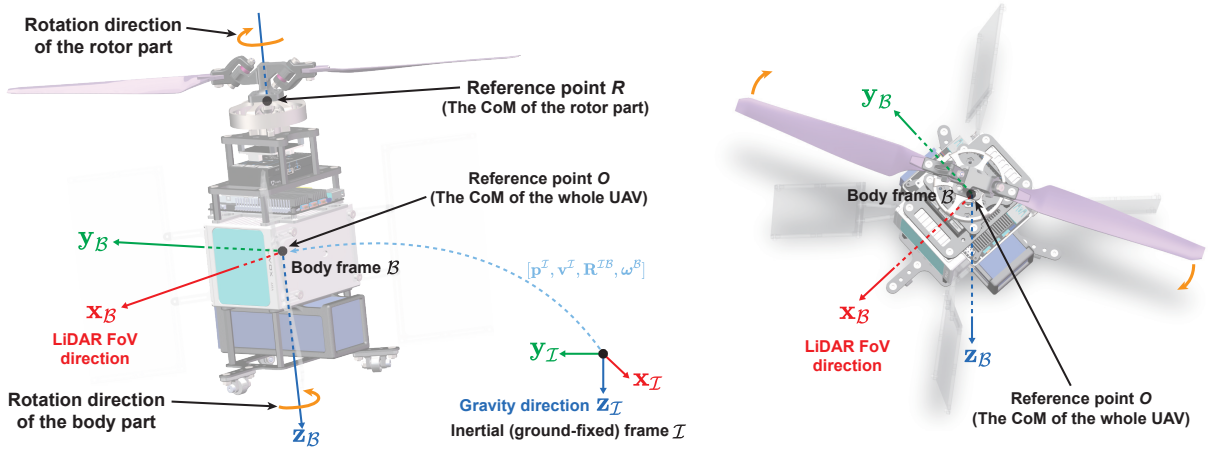

Fig. S11. Definition of coordinate frames and reference points. The reference point R and O are the center of mass (CoM) of the rotor part and the whole UAV (containing both rotor part and body part), respectively.

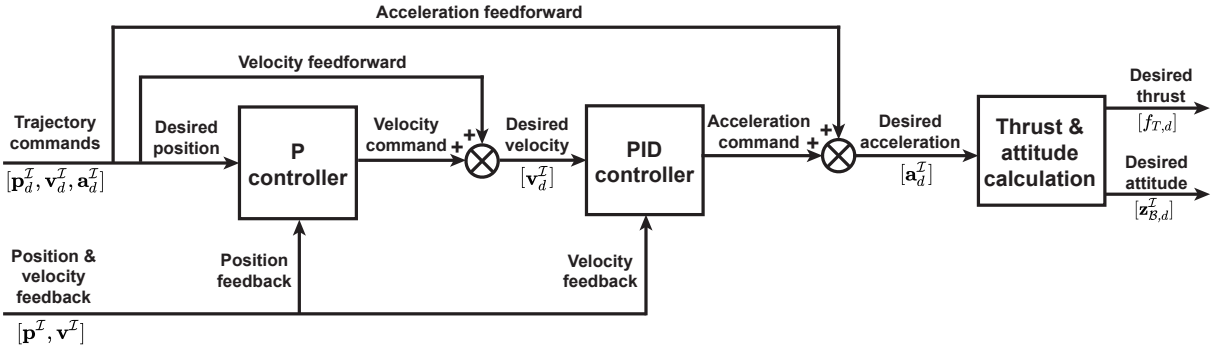

Fig. S12. Structure of the position and velocity controller. A proportional controller is used for position tracking and a PID controller is used for velocity control. The acceleration feedforward of the trajectory is added with the acceleration command computed by the velocity controller to produce the desired acceleration command.

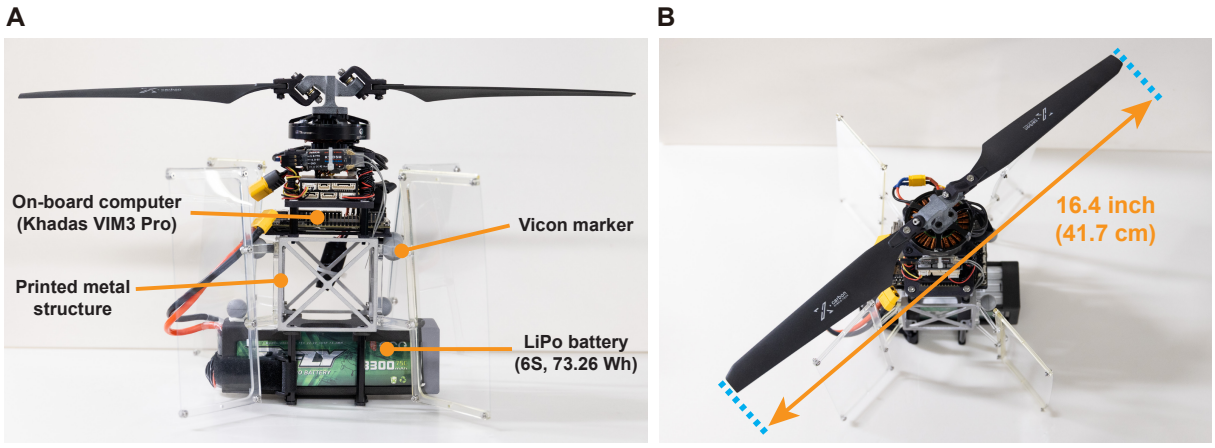

Fig. S13. PULSAR with 16.4-inch propeller and without the LiDAR payload.

Table S1. Specs of PULSAR, the benchmarked UAVs, and commercial UAVs.

UAV type	UAV size (cm × cm)	Propeller diameter (inch)	Total disk area (cm^2)	Battery energy (Wh)	Total weight (g)	Hover power (W)	Hover time	Actual Efficiency (g/W)	Ideal Efficiency (g/W)
PULSAR (Standard)	37.6 x 37.6	14.8	1110.4	41.07	1234	186.5	12 min 42 s	6.65	15.71
PULSAR (no LiDAR)	37.6 x 37.6	14.8	1110.4	41.07	750	91.5	26 min 26 s	8.20	20.15
PULSAR (no LiDAR, 16.4″ propeller)	42.7 x 42.7	16.4	1362.8	73.26	929	113.1	40 min 27 s	8.21	20.05
Benchmarked Quadrotor (7.5″ propeller)	39.9 x 39.9	7.5	1140.1	41.07	1440	254.6	9 min 52 s	5.66	14.73
Benchmarked Quadrotor (8″ propeller)	41.2 x 41.2	8.0	1297.2	41.07	1440	225.5	11 min 03 s	6.39	15.71
DJI Mavic Air 2	43.6 x 36.6	7.2	1050.7	40.42	570	73.5	33 min	7.76	22.48
DJI Mavic 3	58.6 x 52.2	9.4	1790.9	77	895	115.5	40 min	7.75	23.42
DJI Phantom 4 Pro V2.0	48.7 x 48.7	9.4	1790.9	89.2	1375	178.4	30 min	7.71	18.90

Table S2. Comparison of the cyclic speed control performance among different motors. Larger hovering gain is better for cyclic acceleration and deceleration of the motor to drive the swashplateless mechanism.

Motor type	Velocity constant (rpm/V)	Weight (g)	Armature resistance (mΩ)	Maximum battery cells	Time constant (s)	Static gain (rad/s/V)	Hovering gain (rad/s/V)
T-MOTOR MN4004 KV300	300	53	452	6S	0.041	22.37	1.10
T-MOTOR MN4004 KV400	400	53	359	6S	0.052	26.66	1.04
T-MOTOR MN4006 KV380	380	68	194	6S	0.031	31.12	2.03
T-MOTOR MT4006 KV740	740	92	136	4S	0.061	44.52	1.49
T-MOTOR MN5006 KV300	300	108	125	6S	0.014	28.26	3.95
T-MOTOR MN5006 KV450	**450**	**106**	**60**	**6S**	**0.015**	**42.04**	**5.50**
SUNNYSKY V4006 KV320	320	66	230	6S	0.027	27.15	2.03
SUNNYSKY V4006 KV380	380	66	170	6S	0.028	31.99	2.32
SUNNYSKY V4006 KV740	740	68	47	4S	0.029	61.70	4.30
SUNNYSKY V4008 KV380	380	105	131	6S	0.023	33.49	3.00
SUNNYSKY V4008 KV600	600	104	75	4S	0.030	49.53	3.31

Table S3. Components' weight of PULSAR and the benchmarked quadrotors.

UAV type	Single motor (g)	Single propeller with fixture (g)	Single ESC (g)	Propulsion system (g)	Structure (g)	Avionics (g)	Battery (g)	Total weight (g)
PULSAR	107	36	6	149	126	691	268	1234
Quadrotor (7.5″ propeller)	48	23	6	308	168	696	268	1440
Quadrotor (8″ propeller)	48	23	6	308	168	696	268	1440

Table S4. Power consumption of electronic devices on PULSAR and the benchmarked quadrotors.

Device name	Power consumption (W)
Flight controller (Pixhawk 4 Mini)	1.44
LiDAR (Livox AVIA)	6.98
Onboard computer (Khadas VIM3 Pro) (idle)	2.21
Onboard computer (Khadas VIM3 Pro) (loading)	3.80
Total (computer idle)	10.63
Total (computer loading)	12.22

Table S5. Symbol descriptions.

Symbol	Description
η	hover efficiency of a UAV
ρ	air density
m	total mass
A	total propeller disk area
α	current angular position of the rotor
λ_0	angle traversed by the rotor during an acceleration or deceleration
u_t	total throttle, which is the summation of average throttle and sinusoidal component
u_a	average throttle of u_t
u_s	amplitude of the sinusoidal component of u_t
φ	current rotor angle measured by the magnetic encoder
f_T	propeller thrust
M_C	magnitude of the moment produced by the swashplateless mechanism
k_a	constant coefficient of the linear relation between f_T and u_a
k_s	constant coefficient of the linear relation between M_C and u_s
δ	lag angle between the blade and rotor hub during a rotor acceleration
$\mathcal{I}$	inertial (ground-fixed) coordinate frame
$\mathcal{B}$	body-fixed coordinate frame
$\boldsymbol{\omega}^{\mathcal{B}}$	angular velocity vector represented in the body frame $\mathcal{B}$
$\boldsymbol{\omega}^{\mathcal{I}}$	angular velocity vector represented in the inertial frame $\mathcal{I}$
$\mathbf{L}^{\mathcal{I}}$	angular momentum vector represented in the inertial frame $\mathcal{I}$
$\mathbf{R}^{\mathcal{IB}}$	rotation matrix representing the coordinate transformation from $\mathcal{B}$ to $\mathcal{I}$
$\boldsymbol{\Omega}^{\mathcal{B}}$	angular velocity vector of the rotor with respect to the stator
σ	angular speed of the rotor with respect to the stator
$\mathbf{I}_O^{\mathcal{B}}$	inertia matrix of the whole UAV represented in the body frame $\mathcal{B}$
$\mathbf{I}_R^{\mathcal{B}}$	inertia matrix of the rotor part represented in the body frame $\mathcal{B}$
O	CoM of the whole UAV
R	CoM of the rotor part only
$\mathbf{M}^{\mathcal{I}}$	total moment vector represented in the inertial frame $\mathcal{I}$
$\mathbf{M}^{\mathcal{B}}$	total moment vector represented in the body frame $\mathcal{B}$
$M_{\text{prop}}^{\mathcal{B}}$	moment induced by air drag exerted to the rotor part
$M_{\text{body}}^{\mathcal{B}}$	moment induced by air drag exerted to the body part
$\mathbf{z}_{\mathcal{B}}^{\mathcal{I}}$	z-axis of body frame $\mathcal{B}$ represented in the inertial frame $\mathcal{I}$
$\mathbf{z}_{\mathcal{B}}^{\mathcal{B}}$	z-axis of body frame $\mathcal{B}$ represented in the body frame $\mathcal{B}$
$\mathbf{p}^{\mathcal{I}}$	position vector of the UAV represented in the inertial frame $\mathcal{I}$
$\mathbf{v}^{\mathcal{I}}$	velocity vector of the UAV represented in the inertial frame $\mathcal{I}$
$\mathbf{g}^{\mathcal{I}}$	gravity acceleration vector represented in the inertial frame $\mathcal{I}$
g	gravity acceleration
$\mathbf{a}_d^{\mathcal{I}}$	desired acceleration represented in the inertial frame $\mathcal{I}$
$\mathbf{f}_d^{\mathcal{I}}$	desired force represented in the inertial frame $\mathcal{I}$
$f_{T,d}$	desired propeller thrust
$\boldsymbol{\omega}_{xy,d}^{\mathcal{I}}$	desired x- and y-axes angular velocity represented in the inertial frame $\mathcal{I}$
$\boldsymbol{\omega}_{xy,d}^{\mathcal{B}}$	desired x- and y-axes angular velocity represented in the body frame $\mathcal{B}$
k_p^a	proportional gain of the attitude controller
$\mathbf{z}_{\mathcal{B},d}^{\mathcal{I}}$	desired z-axis of the body frame $\mathcal{B}$ represented in the inertial frame $\mathcal{I}$
$\mathbf{M}_{xy,d}^{\mathcal{B}}$	desired moment vector of x-y plane represented in the body frame $\mathcal{B}$
$\tilde{\boldsymbol{\omega}}_{xy}^{\mathcal{B}}$	angular velocity error vector represented in the body frame $\mathcal{B}$
$\mathbf{K}_p^r$	proportional gain matrix of the angular velocity controller
$\mathbf{K}_i^r$	integral gain matrix of the angular velocity controller